J. Fluid Mech. (2003), *vol.* 485, *pp.* 143–159. © 2003 Cambridge University Press
DOI: 10.1017/S0022112003004506 Printed in the United Kingdom

Entrainment and detrainment from a model boundary layer

By MEIHONG SUN AND SETH LICHTER

Department of Mechanical Engineering, Northwestern University, Evanston, IL 60208, USA

(Received 6 January 2002 and in revised form 19 December 2002)

A two-dimensional inviscid flow with piecewise-uniform regions of vorticity is studied as a model of the high-Reynolds-number mixing between a boundary layer and an outer layer. It is found that an initial disturbance to the boundary-layer thickness breaks down into a wave field plus, if the initial disturbance is steep enough, a volume of entrained fluid. The entrained fluid is drawn from the outer layer and then folded into a crevice. The crevice stretches, and eventually pinches off, becoming completely enveloped within the boundary layer. Though the entrained fluid is slender in shape, its volume is significant. Very steep disturbances result in detrainment, in which a small parcel of fluid detaches from the boundary layer and curls into the outer layer. The v-velocity field agrees with many features of Kovasznay *et al.*'s (1970) measurements in the turbulent boundary layer. This correspondence with fully turbulent flow, plus the characteristics of folding and stretching large volumes of fluid, make the process presented here a candidate for a mechanism by which high-Reynolds-number boundary layers mix with outer-layer fluid.

1. Introduction

At high Reynolds numbers, a boundary layer is bounded by a contorted curve. When boundary-layer fluid is dyed to differentiate it from the irrotational flow, flow visualization frequently reveals outer-layer fluid poking deeply into or being completely enveloped within the boundary layer, as well as spires of boundary layer fluid protruding into the outer flow (see figure 1). These intrusions suggest transport due to a convective as opposed to a diffusive mechanism.

To better understand how this type of high-Reynolds-number mixing occurs, we use a model based on formulations of two-dimensional inviscid flow consisting of piecewise-uniform regions of vorticity. The interface between regions of constant vorticity coincides with vorticity jumps. For inviscid flow, the vorticity in each region is invariant (due to Kelvin's theorem), and so the velocity field can be expressed in terms of contour integrals along the vorticity discontinuities (see Zabusky, Hughes & Roberts 1979). The flow evolution, therefore, can be reduced from the two-dimensional Euler's equations to the one-dimensional advection of the contours. Zabusky *et al.* (1979) introduced this type of formulation, called the method of 'contour dynamics'. Later, Dritschel (1988) introduced 'contour surgery' so that the small scales that appeared in contour dynamics computation could be limited through a 'cut-off' scale.

The method of contour dynamics/contour surgery, has been used in many applications; for a review see Pullin (1992). Figure 2 is a summary of the models most relevant to the present study.

https://doi.org/10.1017/S0022112003004506 Published online by Cambridge University Press

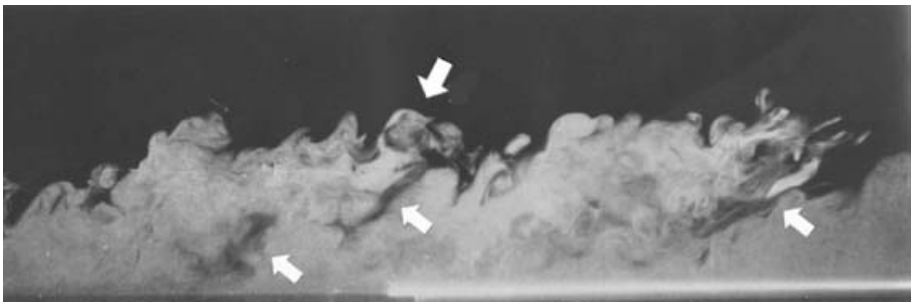


FIGURE 1. A turbulent boundary layer above a solid wall (Falco 1977). The turbulent boundary layer has been filled with 'smoke' composed of small oil particles which appear white by reflecting the light. The dark regions represent the mainly irrotational outer-region fluid. The three lower arrows point to regions of irrotational fluid which have been entrained into the boundary layer (cf. figure 9). The upper arrow indicates what appears to be the breakdown of a wave on the boundary layer into a curl of detrained fluid (cf. figure 11).

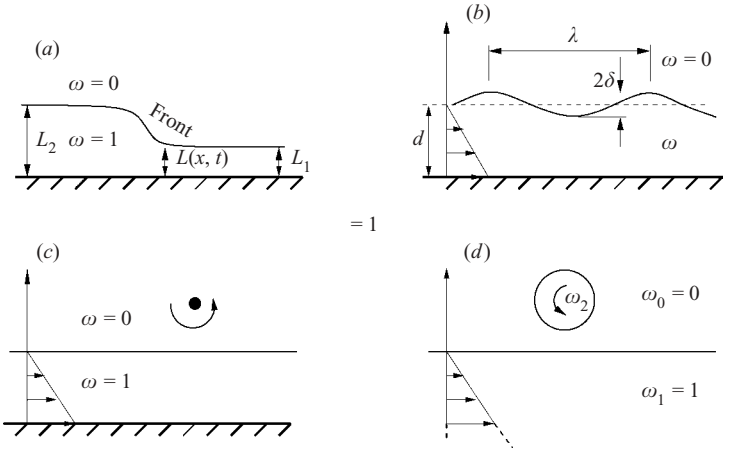


FIGURE 2. Two-dimensional inviscid uniform-vorticity models. (*a*) Stern & Pratt (1985); (*b*) Pullin (1981); (*c*) Atassi *et al.* (1997); (*d*) Stern (1991). In each case, the initial condition is shown. The solid line marks the boundary between rotational $\omega = 1$ and irrotational $\omega = 0$ fluid.

In studying the propagation of vorticity fronts above a wall, Stern & Pratt (1985) found that wave breaking occurs when the front slope exceeds a critical value. Here, 'wave breaking' is said to occur when the initially single-valued vorticity interface $L(x, t)$ (see figure 2*a*) becomes multi-valued due to overturning of irrotational fluid. Despite numerical uncertainty due to low resolution of the numerical method, there was strong evidence that, with the vorticity front as the initial condition, the overturning occurs when $\max \partial L(x, 0)/\partial x$ exceeds a critical value between 0.4 and 0.75. They also showed wave breaking for an isolated bell-shaped disturbance ($L = 1 + 0.5(1 + 100x^2)^{-1}$) when its maximum $\partial L/\partial x$ is sufficiently large and found that the time to breaking is independent of the distance of the lower boundary (wall) from the interface. Subsequent to breaking, irrotational fluid is engulfed into the rotational layer in a very slender crevice.

https://doi.org/10.1017/S0022112003004506 Published online by Cambridge University Press

When the vorticity interface distorts and becomes multi-valued, the distortion may quickly grow intrusively or extrusively such that a filament of fluid with one value of vorticity invades a body of fluid with a different vorticity. This is called filamentation. Pullin (1981) studied the evolution of a wall-bounded vortex layer of mean thickness d due to a finite-amplitude periodic disturbance of wavelength λ and waveheight δ (figure 2*b*). Filamentation is found to be intrusive and occurs when

$$\frac{\delta}{\lambda} \geqslant \frac{1}{4\pi}[1 - \exp(-4\pi d/\lambda)]. \tag{1.1}$$

Notice that the amplitude normalized by λ is a measure of wave steepness, so (1.1) indicates that filamentation occurs when the wave slope is above a certain value.

Atassi, Bernoff & Lichter (1997) studied the interaction of a wall-bounded shear flow with a point vortex, (figure 2*c*). In Atassi, Bernoff & Lichter (1998), the initial conditions (namely, the strength and initial height of the vortex) were chosen such that the initial velocity field induced on the shear flow was approximately invariant except for the x-length scale. Short disturbances propagated slowly and so would remain localized near the vortex, allowing it to wind a thin spire of vortical fluid up and out of the shear layer. On the other hand, if the initial conditions were chosen to produce long disturbances, then a finger of irrotational fluid would be drawn into the shear layer which would align with the wall, implying that the wall (i.e. the image vorticity) plays a role in entrainment.

Stern (1991) (figure 2*d*) studied the interaction of a shear flow with an eddy. Typically, the eddy moves toward the shear flow, and a tongue of rotational flow from the shear flow emerges to wind around the eddy, drawing it and part of the surrounding irrotational fluid into the shear flow.

In the present study, we are interested in the mechanisms of mixing between an irrotational outer region and a boundary layer. We study the evolution of the interface (between irrotational and rotational flow) following an initial disturbance. We uncover a process which can entrain irrotational fluid into the boundary layer and through which the boundary layer loses fluid into the outer region. The model which describes these processes is developed in the following section. Our numerical method is described in § 3. Results are presented and discussed in § 4. The conclusions and our plans for future research are in § 5.

2. Formulation

Reynolds number can be interpreted as the ratio of the time scale $t_\nu \sim H^2/\nu$ on which vorticity diffuses to the time scale $t_\Gamma \sim H^2/\Gamma$ on which vorticity is convected inviscidly by the velocity induced on it (by the Biot-Savart law) due to regions of vorticity of strength Γ. So, for turbulent flow, where $Re \gg 1$, the viscous time scale is much longer than the inviscid time scale, suggesting that boundary-layer vorticity becomes mixed with the outer flow mainly through inviscid interactions. Thus, we consider the model shown in figure 3, in which the flow is divided into two regions: the outer region of irrotational flow with a free-stream velocity U, and the inner region with constant vorticity above a wall. The two regions are separated by an interface located at $y = H(x, t)$, which extends from $-\infty$ upstream to $+\infty$ downstream. The height $H(x, t)$ of the interface denotes the boundary layer thickness.

An inviscid vortex layer of constant height H_∞ would remain unchanged unless disturbed in some manner. We have used two types of initial disturbance. In one, a point vortex is introduced above an initially flat boundary layer (Atassi *et al.* 1997,

https://doi.org/10.1017/S0022112003004506 Published online by Cambridge University Press

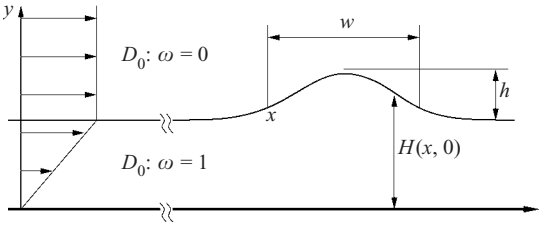


FIGURE 3. A initial Gaussian bump of height h and width w on the interface. The undisturbed interface has a constant height H_∞.

1998). In the other, the initial disturbance is a local thickening of the boundary layer. Our results have shown that either of these two types of initial conditions gives qualitatively similar flow evolution. However, the bump initial condition gives a cleaner view of the evolution process (for example, entrainment into the boundary layer is accompanied by fewer small-scale waves). Therefore (as shown in figure 3), most of our studies used a Gaussian bump (parameterized by its height h and its width w) as the initial condition, and these results are presented here.

The coordinate system places the x-axis along the wall pointing downstream and the y-axis perpendicular to the wall. Variables are non-dimensionalized using the free-stream velocity U, and the initial height of the layer H_∞, such that the undisturbed vortex layer height, the vorticity in the boundary layer and the speed of the initial uniform flow in the outer region all have magnitude one.

The stream function obeys $\nabla^2\Psi = 1$ within the vortical layer $0 < y < H(x,t)$ and $\nabla^2\Psi = 0$ in the outer region $H < y < \infty$ with boundary conditions $\Psi(x,\infty,t) = 0$ and $\Psi(x,0,t) = \text{constant}$. The solution to this problem is

$$\Psi(x,y,t) = \frac{1}{4\pi}\int_{-\infty}^{\infty} \mathrm{d}\xi \int_0^{H(\xi,t)} \mathrm{d}\eta \, \ln\frac{(x-\xi)^2+(y-\eta)^2}{(x-\xi)^2+(y+\eta)^2}, \tag{2.1}$$

where image vortices have been introduced to satisfy the boundary condition at the wall. By expressing $H(x,t)$ as single-valued function of the arclength, s, it is easy to prove that (2.1) and the following equations are valid even if H is a multi-valued function of x. Thus, for any point on the contour $H(x,t)$, the velocity components $u = \partial\Psi/\partial y$ and $v = -\partial\Psi/\partial x$ satisfy

$$u = \frac{\mathrm{d}x}{\mathrm{d}t}, \quad v = \frac{\mathrm{d}H}{\mathrm{d}t}, \tag{2.2}$$

where

$$u = \frac{1}{4\pi}\int_{-\infty}^{\infty} \mathrm{d}\xi \, \ln\frac{\{(x-\xi)^2+[H(x,t)-H(\xi,t)]^2\}\{(x-\xi)^2+[H(x,t)+H(\xi,t)]^2\}}{[(x-\xi)^2+H^2(x,t)]^2}, \tag{2.3}$$

$$v = \frac{1}{4\pi}\int_{-\infty}^{\infty} \mathrm{d}H(\xi,t) \ln\frac{(x-\xi)^2+[H(x,t)-H(\xi,t)]^2}{(x-\xi)^2+[H(x,t)+H(\xi,t)]^2}, \tag{2.4}$$

https://doi.org/10.1017/S0022112003004506 Published online by Cambridge University Press

and where

$$H(-\infty, t) = H(\infty, t) = 1. \tag{2.5}$$

See Atassi *et al.* (1997) for further details.

3. Numerical method

In the contour dynamics/contour surgery numerical method that we use, the interface between the rotational and irrotational flow is discretized into a set of nodes. By fitting a cubic spline to these nodes, an analytical approximation of the interface $H = \{x(s), y(s)\}$ is found from which the arclength s_i and the local curvature $\kappa(s_i)$ at each node can be obtained (for details, see Zabusky *et al.* 1979). The positions of the nodes on the contour have to be readjusted in a smooth way such that the set of nodes can approximate the interface contour with reasonable resolution. So, at every time step, the internodal distance is adjusted according to the magnitude of the local curvature of the interface contour $H(x, t)$ as follows. Starting from one end of the contour, we would like to set the internodal distance, $h_i \equiv s_{i+1} - s_i$ to be inversely proportional to the local curvature, κ_i. But problems arise when a high-curvature region preceeds a low-curvature region (see Dritschel 1988, for details).

To consider the effect of high-curvature regions, a non-local average curvature is defined,

$$\bar{\kappa}_i = \sum_j \frac{d_j |\kappa_j|}{e_{ij}^2} \Bigg/ \sum_j \frac{d_j}{e_{ij}^2} \tag{3.1}$$

where $d_j = \|\boldsymbol{x}_{j+1} - \boldsymbol{x}_j\|$ is the straight-line distance between adjacent modes j and $j+1$, κ_j is the local curvature at node j computed by the cubic spline interpolation, $e_{ij} = \|\boldsymbol{x}_i - \frac{1}{2}(\boldsymbol{x}_j + \boldsymbol{x}_{j+1})\|$ is the distance between node i and halfway between nodes j and $j+1$, and the sum is over all nodes. It is easily seen that the nodes that have large e_{ij} contribute little to the average curvature.

A new curvature for each node can then be determined by

$$\tilde{\kappa}_i = \max[\kappa_i, \bar{\kappa}_i], \tag{3.2}$$

from which a new internodal distance can be found,

$$h_i^* = \frac{c_1}{|\tilde{\kappa}_i|}, \tag{3.3}$$

where $c_1 = 0.2$. This h^* must satisfy

$$h_{min} < h^* < h_{max} \tag{3.4}$$

and

$$(1-r)h_{i-1} < h^* < (1+r)h_{i-1}, \tag{3.5}$$

where the parameter r is 0.3. The lower limit, h_{min}, prevents the number of nodes from growing too rapidly. The upper limit guarantees a minimum accuracy and also helps prevent the contour from being under-resolved. Equation (3.5) allows the internodal distance to change by at most $\pm 30\%$ from one pair of points to the adjacent pair. This control distributes the nodes smoothly on the contour.

After all the nodes have been adjusted, their location along the interface $\{\tilde{s}_i \,|\, 0 \leqslant i \leqslant \tilde{N}\}$ can be used by the cubic spline representation for H to obtain the location of the new nodes $\{\tilde{x}(\tilde{s}_i), \tilde{y}(\tilde{s}_i)\}$, $i = 0, \ldots, \tilde{N}$, where $\tilde{N}$ is the updated number of nodes.

https://doi.org/10.1017/S0022112003004506 Published online by Cambridge University Press

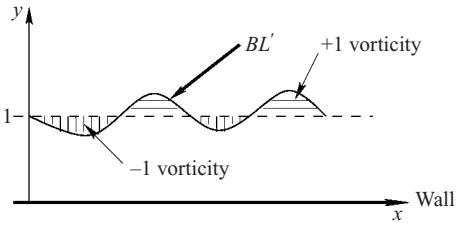


FIGURE 4. The integration region can be viewed as the superposition of the undisturbed vortex layer of unity vorticity and the disturbed region BL' of patches of $+1$-vorticity (above $y=1$) and -1-vorticity (below $y=1$).

The Euler equation does not allow contours to touch or cross (Baker & Shelley 1990). However, it becomes computationally difficult to maintain contours as they become arbitrarily close. Furthermore, the assumption underlying the use of Euler's equation, namely that viscous effects can be neglected, breaks down at these small length scales. So, we impose an artificial local viscosity by merging or breaking contours separated by less than a cut-off distance δ. In our problem, the cut-off scale was set, after trial-and-error, to be one-third of the minimum internodal distance. These small scales do not accumulate a significant amount of vorticity. This form of contour surgery is performed for the following situations. First, when the distance from a node to a non-adjacent point on the same contour is less than δ, the contour is broken into two at this point. Second, when the distance from a node on one contour to a point on a different contour is less than δ, we merge these two contours at this point provided that the two contours bound the same value of vorticity.

The cut-off was most frequently required during entrainment when, as will be seen from the simulations, there is a slender neck of irrotational fluid which extends into the boundary layer. This slender neck may break up into a series of small fragments as the two sides of the neck approach to within the cut-off distance. The frequent use of contour surgery causes a numerical error, discussed below, in which boundary-layer volume, which should be invariant, is lost.

The positions of the nodes are updated by integrating (2.2) using the Adams predictor–corrector method. The u and v velocities are given by the spatial integrals (2.3) and (2.4). Note that the spatial integration is throughout the entire vortex layer. This layer can be viewed as the superposition of the undisturbed vortex layer of constant height and unity vorticity plus a disturbed region BL', as shown shaded in figure 4, of patches of $+1$-vorticity (above $y=1$) and -1-vorticity (below $y=1$). Thus, the numerical integration needs to be carried out only over the limited domain BL' in which the boundary layer is disturbed,

$$u = \begin{cases} y & \text{if } y < H_\infty = 1 \\ 1 & \text{if otherwise} \end{cases} + \frac{1}{4\pi}\int_{BL'} \mathrm{d}\xi \, \ln \frac{[(x-\xi)^2+(H-H')^2][(x-\xi)^2+(H+H')^2]}{[(x-\xi)^2+(H-H_\infty)^2][(x-\xi)^2+(H+H_\infty)^2]}, \quad (3.6)$$

and

$$v = \frac{1}{4\pi}\int_{BL'} \mathrm{d}\xi \, \frac{\partial H'}{\partial \xi} \, \ln \frac{(x-\xi)^2+[H-H']^2}{(x-\xi)^2+[H+H']^2} \quad (3.7)$$

https://doi.org/10.1017/S0022112003004506 Published online by Cambridge University Press

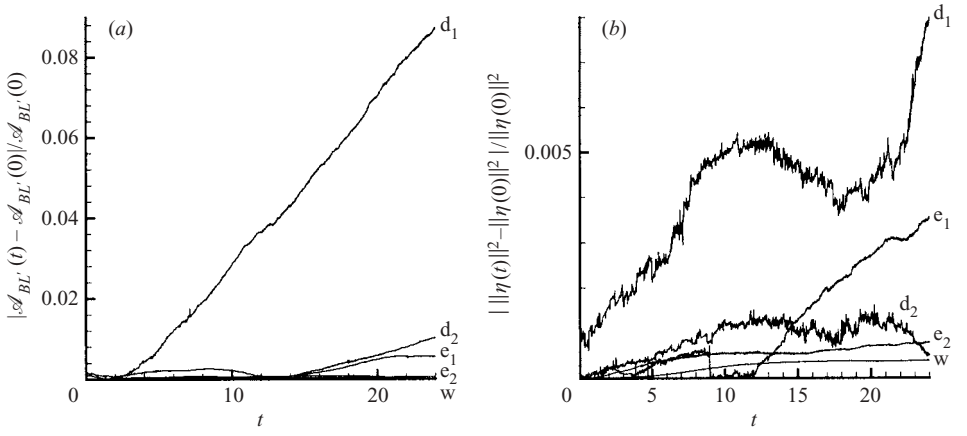


FIGURE 5. The numerical error was monitored by tracking two invariants. (*a*) The relative error $|\mathscr{A}_{BL'}(t)-\mathscr{A}_{BL'}(0)|/\mathscr{A}_{BL'}(0)$, where the integral $\mathscr{A}_{BL'}(t)=\int_{BL'(t)}\mathrm{d}A$ is evaluated only over the volume that is perturbed above or below the otherwise uniform boundary layer thickness, as shown in figure 4. (If the total initial area of the computational domain had been used as the reference area, the values of the relative error would be much smaller.) (*b*) The relative error of the first moment of vorticity $|\|\eta(t)\|^2-\|\eta(0)\|^2|/\|\eta(0)\|^2$, where $\|\eta(t)\|^2=\int y\mathrm{d}A$, and where, as in (*a*), the integral is taken only over BL'. Curve e_1 is the worst case for entrainment, figure 8, which occurs when the entrained volume is small and thin; e_2 shows typical entrainment, corresponding to figure 9; d_1, corresponding to figure 11, is typical of the higher errors during detrainment, though some initial conditions, e.g. $(h, w)=(2.0, 0.2)$ shown as d_2, have lower errors; the error shown by curve w is for the case shown in figure 7 which results in neither entrainment nor detrainment but only waves. In (*a*) curves e_2 and w are indistinguishable from the time-axis.

where $H'=H(\xi,t)$, and $y=H(x,t)$ for nodes on the contour. The limited extent of BL' greatly speeds calculation. Furthermore, the use of the analytic solution for the undisturbed vortex layer extends the computational domain over the entire interval $|x|<\infty$.

For this two-dimensional inviscid incompressible boundary layer, vorticity is an integral invariant, $\int\omega\,\mathrm{d}A=$ constant. As the value of the vorticity ω is constant throughout the domain of integration, the integration volume itself is invariant. The first moment of vorticity is also an integral invariant. (See Batchelor 1967 for a discussion of vorticity invariants.) Numerical fidelity is monitored by tracking the error in these two quantities. In figure 5(*a*), the error is normalized with the volume of the initial disturbance. In all cases of entrainment, this measure of relative error is less than about 0.6%. Even this magnitude of error is unusual and occurs only for entrainment volumes which are exceedingly thin; typically, this measure of error is less than 0.2% during entrainment. Errors during detrainment are typically larger: d_1 shows the worst case in which the error reaches 9% by the time of 24. These large errors are due to regions of high curvature and to the annihilation of fine filaments whose thinness is below the cut-off distance δ. Figure 5(*b*) shows that for both entrainment and detrainment, the error in the first moment of vorticity is always less than 1%. When only waves are generated, as in figure 7 below, the error in either measure never rises above about 0.1%. A more stringent test is to normalize the accumulating error using the entrained or detrained volume, see figure 6. For entrainment, errors are typically less than about 0.5%, with larger errors only when the entrained volume is small, as in e_1. Errors during detrainment can be small,

https://doi.org/10.1017/S0022112003004506 Published online by Cambridge University Press

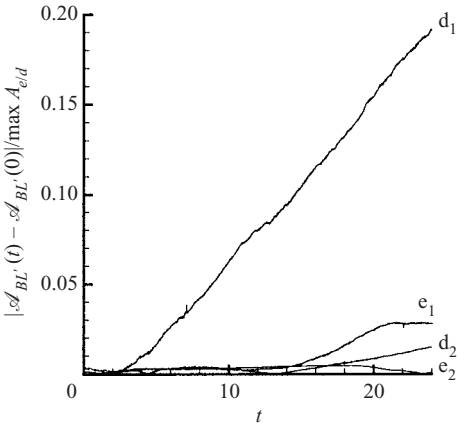


FIGURE 6. The change in the volume of the boundary layer normalized with the maximum entrained (or detrained) volume, $\max A_{e/d}$, provides another measure of error. See the caption of figure 5 for the definition of the volume of the boundary layer $\mathscr{A}_{BL'}(t)$ and the labelling of the curves. Detrainment shows the largest errors due to the small volume of fluid which is detrained from the boundary layer.

as shown by d_2. Typically, however, detrainment, as is apparent from figure 11, is accompanied by very slender filaments which accumulate larger errors, as shown by d_1. Both the high curvature of the filament tips and the smallness of detrained volumes lead to the larger values of the error. However, as for entrainment, the error decreases as detrained volume increases. The time evolution of detrainment, as exemplified in figure 11, is similar for cases with both smaller and larger values of the error; this suggests that the detrainment process may not be qualitatively altered in the presence of the larger values of this particular measure of error. It must be expected, though, that the interface shape near regions of high curvature will not be accurately simulated, and that fine filaments, with thicknesses less than the cut-off value, will be entirely annihilated.

4. Results and discussion

The interface is initially perturbed by a Gaussian of width w and height h,

$$y = 1 + h\exp(-(2x/w)^2), \tag{4.1}$$

centred at $x = 0$. For some initial disturbances, i.e. for some (h, w), the topology of the boundary layer will not change. In figure 7, for $(h, w) = (0.5, 4.47)$, the downstream side of the bump steepens, and irrotational fluid dents into the boundary layer. For times $t \geqslant 12$, the cleft flattens, leaving waves dispersing on the interface.

For other initial disturbances, the topology of the boundary layer will be altered such that the initially singly connected boundary layer envelopes irrotational fluid within it. In figure 8 the initial bump is smaller and narrower, $(h, w) = (0.4, 1.0)$. The downstream side of the disturbance steepens leading to overturning and the production of a crevice pointing into the vortex layer (at $t = 4$). The interface and the irrotational fluid within the crevice have been folded through nearly 180°, see $t = 8$. The crevice continues to stretch, dragging irrotational fluid deep into the boundary layer. At $t = 12$, the tip of the irrotational fluid has reached $y = 0.4$, and the crevice has a length of approximately 4, i.e. 4 times the boundary layer thickness. At

https://doi.org/10.1017/S0022112003004506 Published online by Cambridge University Press

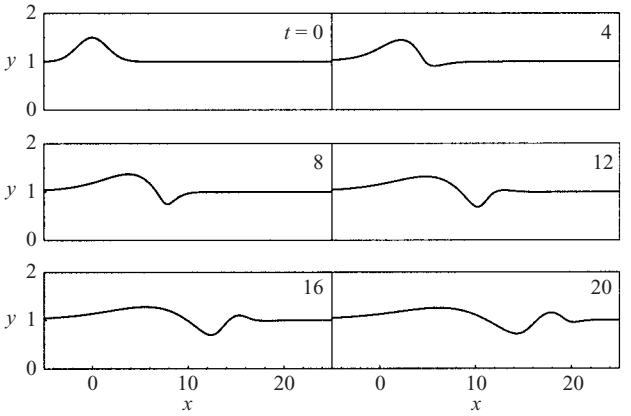


FIGURE 7. The evolution of the interface subject to an initial disturbance in the form of a Gaussian bump of height $h = 0.5$ and width $w = 4.47$, for six times $0 \leqslant t \leqslant 20$. The downstream coordinate is x. The undisturbed boundary layer height is unity. Note the stretched scale in x. A wave is generated on the interface and no entrainment occurs.

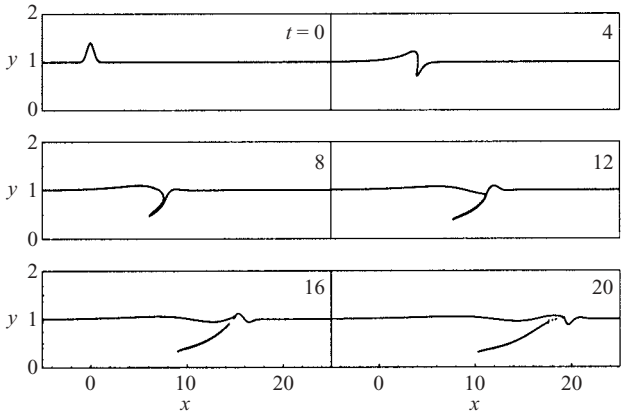


FIGURE 8. As figure 7 but for an initial disturbance $(h, w) = (0.4, 1.0)$. Irrotational fluid from the outer region is drawn into the boundary layer in a narrow crevice which pinches off at $t \approx 15$. The entrained fluid is completely enveloped within the boundary layer, as can be seen at $t = 16, 20$.

approximately $t = 15$, the crevice of irrotational fluid is pinched off and is enveloped within the boundary layer. This process of drawing in and enveloping irrotational fluid within the boundary layer is called entrainment. That is, entrainment is associated with a change of topology from a simply connected boundary layer to one which is multiply connected. The top portion of the crevice convects downstream with nearly the free-stream speed, while portions close to the wall are proportionally slower. Hence, the two ends of the bolus are stretched: at $t = 16$, the crevice has an extent in the x-direction of approximately 6; subsequently, at $t = 20$, the length of the entrained crevice is about 8.

Figure 9 shows the evolution of the interface with an initial disturbance of $(h, w) = (0.8, 2.0)$. As in the previous case, the irrotational fluid is folded and drawn deep into the boundary layer by the overturning bump. At $t = 8$, the tip of the crevice of irrotational fluid has reach down to $y = 0.3$. At approximately $t = 14.5$, the crevice

https://doi.org/10.1017/S0022112003004506 Published online by Cambridge University Press

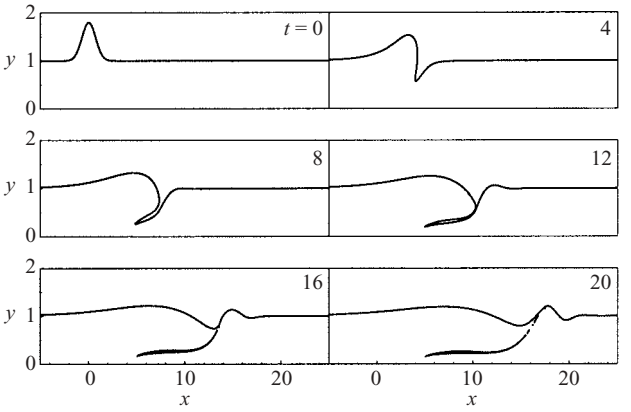


FIGURE 9. As figure 7 but for an initial disturbance $(h, w) = (0.8, 2.0)$. Entrainment of irrotational fluid into the boundary layer occurs as in figure 8, though here the volume of entrained fluid is larger.

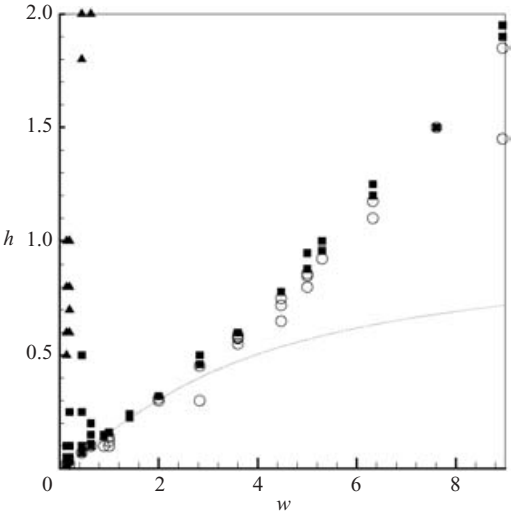


FIGURE 10. Transition boundary of entrainment. Squares show the initial disturbances for which entrainment occurs; circles show those for which no entrainment occurs. The dotted line is the transition boundary from Pullin (1981), (1.1). Triangles show initial disturbances for which detrainment occurs.

pinches off into a bolus of entrained fluid. This bolus is stretched so that at $t = 16$ its length along the x-direction is approximately 7. By $t = 20$, most of the entrained fluid lies in a thin layer aligned with the flow direction near $y = 0.25$. The upper part of the bolus has fragmented into a chain of small pieces which drift upward to rejoin the upper layer. Compared with the case in figure 8, the entrained volume of the irrotational fluid in this case is much larger and the bolus of entrained fluid lies deeper within the boundary layer.

Figure 10 presents the stability boundaries for entrainment. The abscissa and ordinate are the width w and the height h, respectively, of the initial disturbance. The squares show those disturbances which result in entrainment; circles show cases

https://doi.org/10.1017/S0022112003004506 Published online by Cambridge University Press

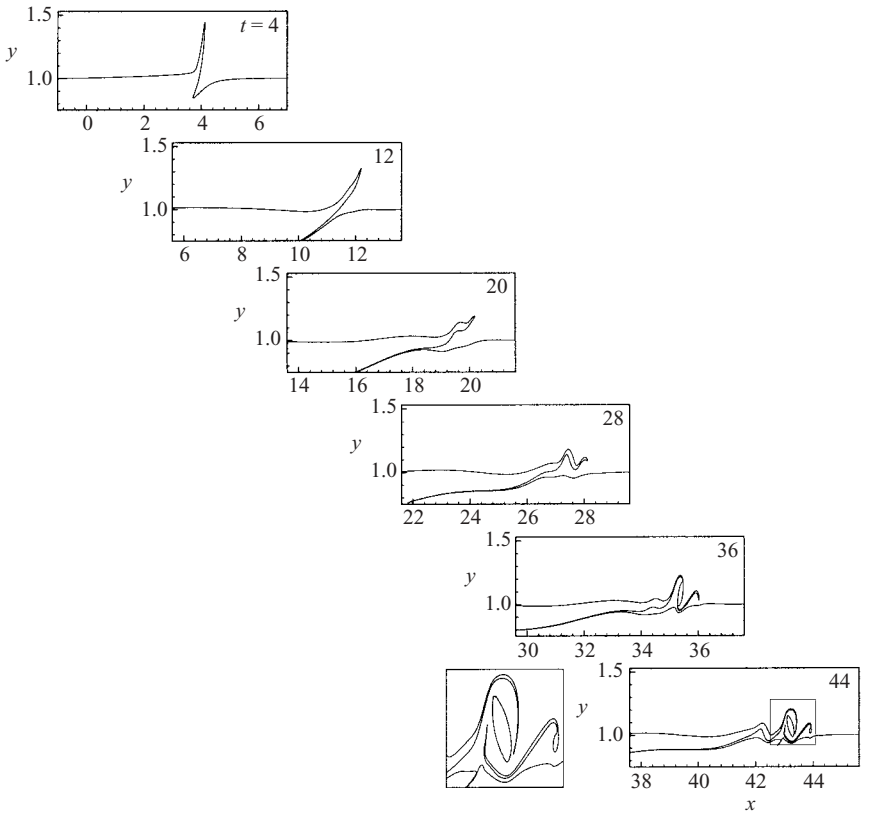


FIGURE 11. Detrainment of rotational fluid out of vortex layer for initial disturbance $(h, w) = (0.5, 0.1414)$. Results are shown for six times for $8 \leqslant t \leqslant 44$. At $t = 44$, the detrainment structure is magnified for a better view.

with no entrainment. Pullin (1981) and Pullin *et al.* (1989), in studying a vortex layer with a periodic initial disturbance, find that a minimum amplitude of disturbance is required for filamentation to occur. In order to compare the results from our compact disturbance to those of Pullin, we set $\lambda = 2w$. For narrow Gaussian disturbances, i.e. $w \lesssim 2$, entrainment is consistent with the linear stability boundary found by Pullin (1981), (1.1). For broader disturbances, i.e. $w \gtrsim 2$, the instability limit no longer falls along the linear stability boundary, but lies near the line $h/w \sim 0.16$.

The triangles in figure 10 mark disturbances which result in another phenomenon, shown in figure 11. The initial disturbance, $(h, w) = (0.5, 0.1414)$, has the same height as in the case in figure 7 but is very narrow. The crevice due to the steepening of the downstream side of the initial disturbance is very shallow and does not pinch off at later times. Instead, the initial bump (now a slender finger intruding into the outer layer) develops waviness and collects portions of rotational fluid into a small bolus which is pinched off at a later time ($t = 44$) causing the rotational fluid inside to be left surrounded by the outer layer. This process is what we call detrainment. That is, a region of rotational fluid detaches from the bulk of the boundary layer to be enveloped by irrotational fluid.

As can be seen from figures 8 and 9, the entrained volume is slender. For example, its aspect ratio in figure 9 at $t = 20$ is approximately 1:100. Despite its thinness, the

https://doi.org/10.1017/S0022112003004506 Published online by Cambridge University Press

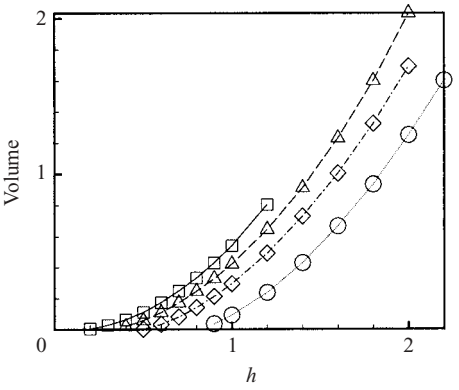


FIGURE 12. The volume of entrained fluid for four different widths of the initial Gaussian. □, $w=1$; △, $w=2$; ◇, $w=3$; ○, $w=4.47$.

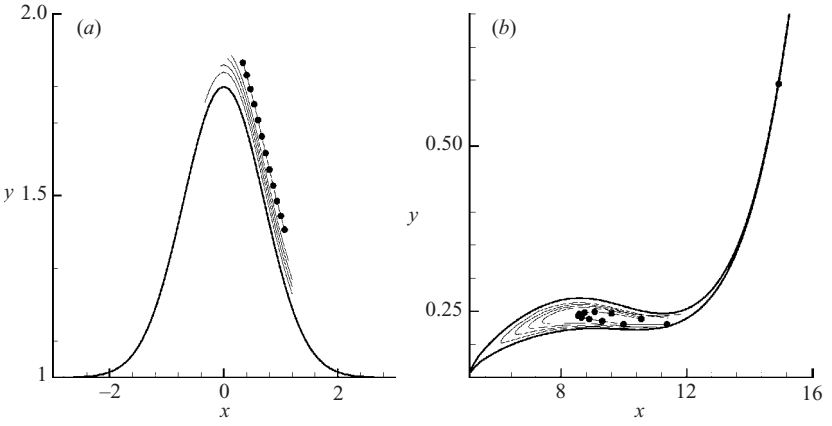


FIGURE 13. For the case shown in figure 9, the initial distribution of five chains of fluid at $t=0$ which are subsequently entrained is shown in (*a*). At $t=16$, after being folded and stretched, the markers are arrayed as in (*b*). The heavy line in each figure shows the position of the interface and the chain farthest from it is divided into segments by Lagrangian markers.

entrained bolus can contain a significant amount of irrotational fluid. Figure 12 shows the volume of entrained irrotational fluid as a function of initial height h for four different values of initial width w. Here, the volume is defined in terms of the area of the bolus of irrotational fluid when it first pinches off from the interface and is enveloped by the boundary layer. A value of unity indicates that the bolus contains a volume equal to that in a square whose sides are of length equal to the boundary layer thickness. The volume increases with the height h, but decreases with the width w.

From where does the entrained fluid arise? To answer this question, chains of Lagrangian particles were arrayed in the irrotational fluid and their positions tracked. For the case shown in figure 9, figure 13(*a*) shows the initial position of the five chains which at $t=16$ were entrained into the bolus. For the chain furthest from the interface in figure 13(*a*), Lagrangian markers, which break the chain into eleven segments, are also shown. The entrained chains are folded, see figure 13(*b*), at approximately the positions where the initial lines have maximum slope.

https://doi.org/10.1017/S0022112003004506 Published online by Cambridge University Press

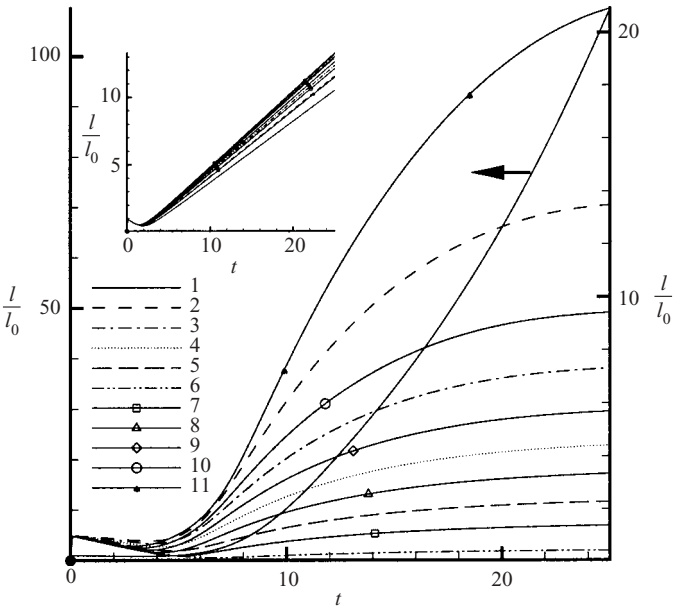


FIGURE 14. The length l, normalized with respect to initial length l_0, as a function of time for each segment between the Lagrangian markers of the fluid chain shown in figure 13: the segments are numbered according to their initial locations (as shown in figure 13*a*) from left to right and top to bottom along the chain. The result for Segment 1 uses the ordinate on the left. For comparison, the inset shows how line segments with the same initial orientation would be stretched by a uniform shear flow of unity vorticity.

The fluid within the entrained volume is not only folded, but also stretched. To quantify the stretching, we measure the length of the line segments between pairs of Lagrangian markers. Figure 13 explicitly shows those markers for one of the fluid chains. Figure 14 shows the length l of each of the eleven segments, normalized with respect to its initial length l_0. For comparison, the inset shows how line segments with the same initial orientation would be stretched by a uniform shear flow of unity vorticity: after an brief interval of compression, all segments are linearly stretched. The segments in the boundary layer flow also undergo an initial compression followed by stretching. However, in general, by time $t = 20$ most segments have been folded into a thin layer centred at $y = 0.25$ for which the u-velocity is nearly constant, and hence stretching ceases. Segment 1 lies in the upstream tail which curves upward and so the relative velocity between its upper and lower ends maintains the stretch.

Figure 15 shows the flow field at time $t = 20$ for $(h, w) = (0.8, 2.0)$. Streamlines are shown by contours with arrows; curves of constant u-velocity are labelled with the value of u, and the interface is superimposed as a heavy solid curve. As entrainment occurs, the entrained fluid, initially at near free-stream speed, decelerates to the speed of the surrounding flow. This is just what one might expect from mixing-length arguments. Consequently, the presence of the entrained fluid can hardly be detected by looking at the streamlines. On crossing into the entrained volume, lines of constant u-velocity are kinked such that the u-velocity appears constant for fixed x-location. However, these kinks are actually quite small: note that in figure 15 the y-scale has been expanded by a factor of approximately 50 in comparison with the x-scale.

https://doi.org/10.1017/S0022112003004506 Published online by Cambridge University Press

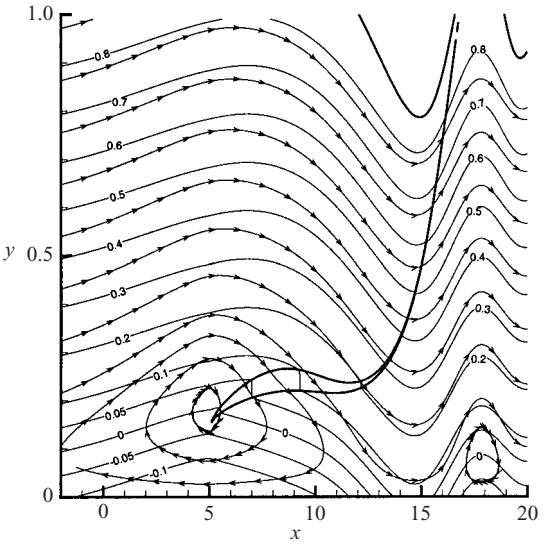


FIGURE 15. The flow field near the entrained fluid region at $t = 20$ for the case with $(h, w) = (0.8, 2.0)$ (see figure 9). The interface contour (heavy solid curve) has superimposed u-velocity contours (solid curves) and streamlines (curves with arrows).

Pullin studied the constant-vorticity boundary layer disturbed by waves, rather than the compact disturbances as here (Pullin 1981; Pullin *et al.* 1989). He found that, if of sufficient steepness, the waves would increase in amplitude and evolve such that they were rounded at their crests and narrow at the troughs, the angle of the filament was about 15°, the fronts of bulges propagated faster than their backs, and the wave speeds were slightly less than the free-stream velocity. All these findings are in agreement with measurements of bulges in a turbulent boundary layer (Kovasznay, Kibens & Blackwelder 1970). To further test the similarity between the entrainment process and boundary-layer bulges, we compared the v-velocity field of the evolving disturbance with measurements in the turbulent boundary layer as shown in figure 16. Our data are conditionally sampled and normalized in the same manner as the turbulent data. Specifically, a numerical trigger probe was placed at a height y_D. When this probe detected the passage of the contour separating irrotational from rotational fluid, the v-velocity is measured at a second probe at height y. Each line of data corresponds to a different value of y_D conditioned on being at the 'back' or 'front' of the disturbance. Passing from irrotational to rotational flow (rotational to irrotational) denotes the front (back) of the disturbance. The y-scale was normalized with respect to the boundary-layer height and the v-velocity scale was normalized with respect to the free-stream velocity. The heights of the trigger probes, relative to the boundary-layer height, in both sets of data are the same, so the data in figures 16(a) and 16(b) can be compared line-by-line. Note, though, that Kovasznay *et al.*'s data are for the ensembled-averaged 'bulge', while the present data are for a single disturbance $(h, w) = (0.1, 2.0)$ at time $t = 2$. The two sets of data, one from the turbulent boundary layer and the other from the present model, are similar in form and scale. In particular, on the backs of the disturbance: (i) non-zero velocities range over $-1.0 \lesssim Y \lesssim 1.0$, (ii) the maximum magnitudes fall near $Y = 0$, (iii) both positive and negative velocities occur, (iv) the maximum positive velocity is about 0.01, and (v) the minimum value

https://doi.org/10.1017/S0022112003004506 Published online by Cambridge University Press

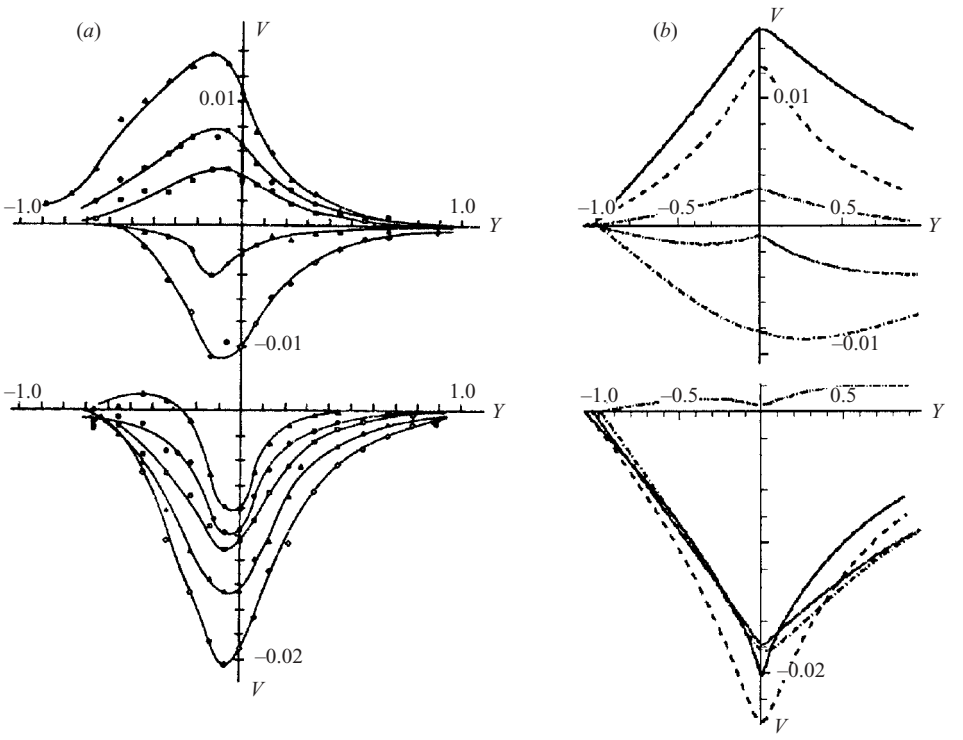


FIGURE 16. Conditionally averaged v-velocity profiles: (a) results from Kovasznay *et al.* (1970) and (b) from the current study. In all cases, the abscissa, $Y = y - y_D$, has been normalized with respect to the boundary-layer thickness, where y_D is the height of the trigger probe which detects the passage of the contour separating vortical from irrotational fluid. On detection, a second probe records the v-velocity at height y. The measured velocity (minus the mean v-velocity) is normalized in all cases with respect to the free-stream velocity and shown as V. Kovasznay *et al.*'s data are for the ensembled-averaged 'bulge'. The present data are for a single disturbance $(h, w) = (0.1, 2.0)$ at time $t = 2$. Each line corresponds to a different value of y_D conditional on its being on a back (upper two plots) or a front (lower two plots) of a disturbance.

of the negative velocity is about -0.01. On the fronts, both sets of data show: (i) non-zero velocities in the range $-1.0 \lesssim Y \lesssim 1.0$, (ii) the maximum magnitudes fall near $Y = 0$, (iii) almost exclusively negative velocities with the exception of one line with small positive velocities, and (iv) the minimum value of the negative velocity is about -0.02.

5. Conclusions

This work considers a model high-Reynolds-number boundary layer. It is shown that a local thickening of the boundary layer breaks down into a wave field plus, if the initial disturbance is steep enough, $h/w \gtrsim 0.16$, a volume of entrained fluid. The entrained fluid is drawn from the irrotational outer region and folded into the boundary layer, first forming a crevice which points nearly normal to the wall and subsequently is stretched along the flow direction. The entrained volume of irrotational fluid can become very slender, reaching aspects ratios in which its width is only $O(0.01)$ of its length. The attributes of folding and stretching suggest that the

https://doi.org/10.1017/S0022112003004506 Published online by Cambridge University Press

entrainment process would facilitate molecular mixing. The bolus of entrained fluid is completed engulfed within the boundary layer, often at a deep level, within the 25% of the boundary layer closest to the wall. The volume of entrained fluid is large, of $O(1)$.

Relatively thin initial disturbances lead to detrainment, in which vortical fluid from the boundary layer detaches from the bulk of the boundary-layer fluid and becomes surrounded by the irrotational fluid of the outer region. Detrained volumes are typically much smaller than entrained volumes.

The 'bulges' seen in turbulent boundary layers appear similar to these model disturbances. Here, we show that the disturbances generate conditionally averaged v-velocity profiles which are similar to those found in the turbulent bulges. The comparison is not strictly valid, as the turbulent data are for the ensemble of large and small, and young and old structures which pass the measuring stations, while our results are for a single realization. To generate a set of disturbances equivalent to Kovasznay's bulges would require generating the disturbances from a set of background fluctuations, rather than from a finite-amplitude initial condition, as done here.

This work used the Lagrangian technique of contour dynamics/contour surgery which explicitly tracks the contour separating vortical from irrotational fluid. Eulerian measures, such as the velocity field, would not so clearly differentiate the entrained volume. Furthermore, the slender shape of the entrained volume would make it easy to overlook in physical measurement or in numerical simulations which present only streamlines.

The ultimate objective of this work is to better understand transport into the high-Reynolds-number boundary layer. The results of this work suggest that this model may capture some of the features of the mechanism by which transport into and out of the high-Reynolds-number boundary layer occurs. The model has only two parameters, namely the height and width (h, w) of the initial disturbance. The choice of (h, w) sets whether entrainment, detrainment or only waves will evolve. One can imagine, on looking at flow visualizations such as figure 1, that the ragged edge of the boundary layer is a superposition of these three types of disturbances. If so, transport coefficients into the boundary layer, and the velocity fluctuations, Reynolds stresses and the mean (log and wake) profiles near the outer edge of the boundary layer might be described by the collective action of the entrainment, detrainment and waves contained in this model. Our future work will explore these possibilities.

The financial support of the National Science Foundation, CTS-9729190, is gratefully acknowledged.

REFERENCES

Atassi, O. V., Bernoff, A. J. & Lichter, S. 1997 The interaction of a point vortex with a wall-bounded vortex layer. *J. Fluid Mech.* **343**, 169–195.

Atassi, O. V., Bernoff, A. J. & Lichter, S. 1998 Interacting vortex and vortex layer: how length scale affects entrainment and ejection. *AIAA J.* **36**, 924–928.

Baker, G. R. & Shelley, M. J. 1990 On the connection between thin vortex layers and vortex sheets. *J. Fluid Mech.* **215**, 161–194.

Batchelor, G. K. 1967 *An Introduction to Fluid Dynamics*. Cambridge University Press.

Dritschel, D. G. 1988 Contour surgery: a topological reconnection scheme for extended integrations using contour dynamics. *J. Comput. Phys.* **77**, 240–266.

https://doi.org/10.1017/S0022112003004506 Published online by Cambridge University Press

Falco, R. E. 1977 Coherent motions in the outer region of turbulent boundary layers. *Phys. Fluids* **20**, S124–S132.

Kovasznay, L. S. G., Kibens, V. & Blackwelder, R. F. 1970 Large-scale motion in intermittent region of a turbulent boundary layer. *J. Fluid Mech.* **41**, 283–325.

Pullin, D. I. 1981 The nonlinear behaviour of a constant vorticity layer at a wall. *J. Fluid Mech.* **108**, 401–421.

Pullin, D. I. 1992 Contour dynamics methods. *Annu. Rev. Fluid Mech.* **24**, 89–115.

Pullin, D. I., Jacobs, P. A., Grimshaw, R. H. J. & Saffman, P. G. 1989 Instability and filamentation of finite-amplitude waves on vortex layers of finite thickness. *J. Fluid Mech.* **209**, 359–384.

Stern, M. E. 1991 Entrainment of an eddy at the edge of a jet. *J. Fluid Mech.* **228**, 343–360.

Stern, M. E. & Pratt, L. J. 1985 Dynamics of vorticity fronts. *J. Fluid Mech.* **161**, 513–532.

Zabusky, N. J., Hughes, M. H. & Roberts, K. V. 1979 Contour dynamics for the Euler equations in two dimensions. *J. Comput. Phys.* **30**, 96–106.

https://doi.org/10.1017/S0022112003004506 Published online by Cambridge University Press